

# Dynamics Identification of a Damped Multi Elastic Link Robot Arm under Gravity

Jörn Malzahn<sup>1</sup>, René Felix Reinhart<sup>2</sup> and Torsten Bertram<sup>1</sup>

**Abstract**—The infinite dimensionality, varying, uncertainties or even unknown boundary conditions render the derivation and - in particular - the identification of accurate dynamics models for elastic link robots tedious and error prone. This contribution circumvents these challenges by the prior application of a model-free inner loop oscillation damping controller before modelling the robot's dynamics. Then, the damped dynamics of a multi elastic link robot arm under gravity can be modelled with high accuracy. An analytical and a data-driven model for the damped dynamics are proposed and quantitatively compared. Both models can explain motor currents as well as link strain measurements in real-time. The paper includes an experimental model validation with different payloads in the entire workspace of the robot.

## I. INTRODUCTION

The preservation of rigidity in economic lightweight structures is a mechanical design challenge. If elasticity is inevitable or if intrinsic compliance is an application-specific requirement, sophisticated control algorithms have to be devised in order to suppress oscillations and achieve accurate positioning. This is the focus of the present literature on the control of elastic link robots. However, the exploitation of the intrinsic compliance, for example to enable force control, is often neglected. Experimental works such as [1], [2] are rare. The influence of gravity is frequently excluded. Even fewer papers consider multi-link arms [3], [4] under gravity.

The reason for that is most probably the complexity of the elastic link dynamics. To accurately model the distributed oscillatory dynamics, a fourth order partial differential equation has to be solved for each elastic link. Common modelling formalisms involve a truncation of the actually infinite system order to a finite number of assumed modes [5]. In general, the boundary conditions associated with each partial differential equation vary with the joint configuration [6]. A modification to the boundary conditions affects the mode shapes and shifts the oscillation frequencies. While imperfect clamping already adds uncertainty to the boundary conditions, a change in the payload or eventual physical contacts with the environment introduce arbitrary, generally unknown boundary conditions. Against this background it is very hard to derive and - in particular - to identify a holistic dynamics model, which accurately explains the link oscillations in the entire operation range of a real robot. Most likely such a model lacks real-time capabilities.

<sup>1</sup>Jörn Malzahn and Torsten Bertram are with the Institute of Control Theory and Systems Engineering, Technische Universität Dortmund, 44227 Dortmund, Germany. joern.malzahn@tu-dortmund.de

<sup>2</sup>Felix Reinhart is with the Research Institute of Cognition & Robotics - CoR-Lab, Bielefeld University, Bielefeld, Germany. freinhar@cor-lab.uni-bielefeld.de

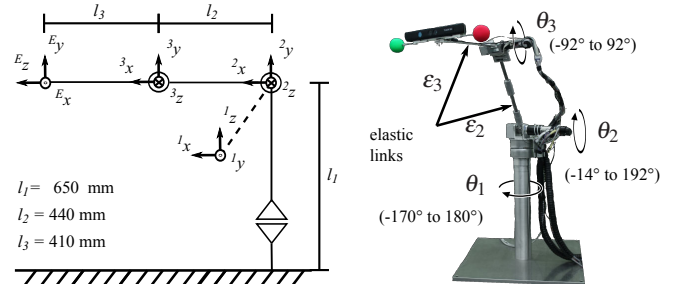


Fig. 1. Equivalent rigid body kinematics (left) and photograph (right) of the 3 DOF experimental setup TUDOR (Technische Universität Dortmund Omnielastic Robot).

This contribution proposes to circumvent the majority of the aforementioned challenges for system identification of elastic link robots by prior application of an inner loop oscillation damping controller. It ties in with the authors previous work on the model free independent joint oscillation damping controller presented in [4]. The model free controller rapidly damps link oscillations with tip amplitudes of about 10 cm. It preserves the speed of motion and enables the elastic link robot to catch multiple balls subsequently thrown by a human [7]. On top of the actively damped elastic link dynamics, this paper presents two real-time capable models for the remaining dynamics. Both models are identified and validated by experiments with multiple payloads under gravitational influence. The first model is analytically derived through the investigation of the load torque distribution in the links. The second one is a data-driven neural network and models the same output using “problem agnostic” features. Both models describe the same dynamics structure, work on exactly the same input/output data and are efficiently identified using linear regression techniques to explain the per link strain measurements or the per joint motor currents. An analytical model is generally preferred for control. However, the capability of the neural network to approximate arbitrary nonlinear functions provides a benchmark for the analytical model. The validation experiments are conducted with the multi-link experimental setup TUDOR depicted in Fig. 1.

The next section introduces the experimental setup and exemplifies the oscillation damping. Section III derives the analytical model and explains the applied neural network. The identification experiments and results are discussed in section IV. The paper concludes and gives an outlook in section V.

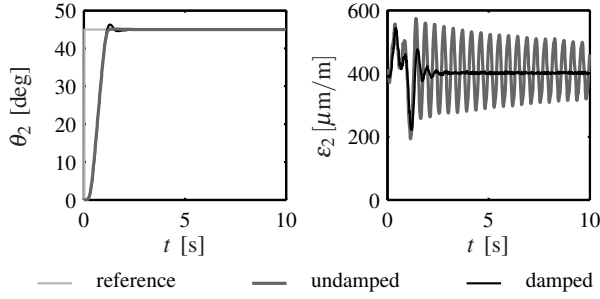


Fig. 2. Damping of link oscillations induced by a joint motion from  $\theta = [0^\circ, 0^\circ, 0^\circ]^T$  to  $\theta = [0^\circ, 45^\circ, -45^\circ]^T$ . Second joint angle  $\theta_2$  (left) and link strain  $\epsilon_2$  (right) measured close to the hub on the second link.

## II. EXPERIMENTAL SETUP

The elastic link robot TUDOR is depicted in Fig. 1 along with the equivalent rigid body kinematics. The actuators are three brushless DC motors with planetary gears. The gear ratios are 156:1, 230:1 and 246:1 in the order from the first to the third joint. The vendor specifies a backlash of less than 1 degree. The joint encoders have a resolution of 500 impulses per revolution. The first motor is located in the cylindrical base and actuates the robot about the vertical axis  $^1\mathbf{z}$  by the joint angle  $\theta_1$ . The second and third motors operate about the horizontal axes  $^2\mathbf{z}$  and  $^3\mathbf{z}$  by the joint angles  $\theta_2$  and  $\theta_3$ . The fixture between the first and second joint is considered to be the first link body. The second link body is a spring steel blade of 4 mm height and 15 mm width. An identical spring steel blade is mounted to the shaft of the third joint. The mass of each spring steel blade amounts to 185 g. Both elastic links are equipped with two pairs of strain gauges. The pair close to the preceding joints is used in this work. The blades orientation is selected so that the deflections and oscillations predominantly occur in the vertical  $^2\mathbf{x} - ^2\mathbf{y}$ -plane. Therefore, gravitational effects have to be considered because static deflections depending on payload and joint configuration occur. Depending on the payload, joint configuration and acceleration profile, the tip oscillations are in the range of 10 cm. The dominant eigen frequencies observable on both elastic links range between 1 and 13 Hz accordingly. Based on the author's previous work in [4], the oscillations are actively damped using a cascaded independent joint control concept augmented by a linear mean deliberated strain feedback. Figure 2 exemplifies the rapid oscillation damping of this scheme.

Figure 1 shows an eye-in-hand mounted camera and spheres for end effector tracking with an external measurement setup. Within the scope of this work, these devices are replaced by steel plates with dimensions 80 by 80 by 2 mm<sup>3</sup> and mass of 100 g. By adding such steel plates, the dynamics modelling approaches presented in this work are investigated for payloads  $m_L$  between 0 and 400 g.

The computer running the controllers and dynamics models is a standard PC with a 3.8 GHz Pentium 4 processor, 2048 MB RAM, a Humusoft MF624 I/O board and 0.5 ms sampling rate.

## III. DYNAMICS MODELLING

### A. The Motor Currents

The torque balance at the shaft of each individual actuator yields:

$$\tau_E = \tau_M + \tau_F + \tau_J. \quad (1)$$

The controlled motor current  $i_M$  generates the electrical torque  $\tau_E = k_\tau i_M$  with the motor torque constant  $k_\tau$ . The mechanical torque  $I_M^{-1} \tau_M = \ddot{\theta}$  accelerates the joint rotor inversely proportional to the rotor inertia  $I_M$ . The joint friction  $\tau_F$  is modelled by

$$\tau_F = k_v^+ + (k_v^- - k_v^+) f_1(\dot{\theta}) + k_c^+ + (k_c^- - k_c^+) f_2(\dot{\theta}), \quad (2)$$

with

$$f_1(\dot{\theta}) = \begin{cases} 0 & \text{if } \dot{\theta} \geq 0 \\ \dot{\theta} & \text{if } \dot{\theta} < 0 \end{cases} \quad (3)$$

and

$$f_2(\dot{\theta}) = \begin{cases} 0 & \text{if } \dot{\theta} \geq 0 \\ 1 & \text{if } \dot{\theta} < 0. \end{cases} \quad (4)$$

The parameters  $k_v^+$  and  $k_v^-$  denote the velocity direction dependent viscous friction coefficients while  $k_c^+$  and  $k_c^-$  are the corresponding coulomb friction coefficients.

Let the vector  $\tau_J$  collect the load torques on all joints. These load torques originate from the motions of the robot arm bodies:

$$\tau_J = \mathbf{I}(\mathbf{q})\ddot{\mathbf{q}} + \mathbf{C}(\mathbf{q}, \dot{\mathbf{q}})\dot{\mathbf{q}} + \mathbf{g}(\mathbf{q}), \quad (5)$$

where  $\mathbf{I}$  denotes the symmetric positive definite robot inertia matrix. The matrix  $\mathbf{C}$  collects the Coriolis and centrifugal terms. The vector  $\mathbf{g}$  describes the load torque due to gravity.

The expressions for the mechanical torque  $\tau_M$ , the friction torque  $\tau_F$  as well as the load torque  $\tau_J$  are all linear in their parameters. With this insight, equation (1) can be rearranged to formulate the parameter identification task from experimental data in terms of the linear regression problem

$$\mathbf{i}_M = \mathbf{Y}_i(\mathbf{q}, \dot{\mathbf{q}}, \ddot{\mathbf{q}}) \boldsymbol{\chi}_i. \quad (6)$$

The vector  $\mathbf{i}_M$  collects the motor currents measurable at each individual joint. The regressor  $\mathbf{Y}_i$  solely depends on the joint motion. The vector  $\boldsymbol{\chi}_i$  collects the minimal set of identifiable base dynamics parameters. Two symbolic and one numerical approach for finding the base parameters are described in [8]. This work follows the numerical approach analyzing the space span by the columns of  $\mathbf{Y}_i$  and solves equation (6) using a linear least-squares technique.

### B. The Link Strains

The derivation of a model for the link strains is based on the difference between the load torque  $\tau_L(x)$  experienced at each individual joint shaft  $\tau_J = \tau_L(0)$  and the load torque  $\tau_L(x_s)$  causing the strain measured at a strain gauge position  $x_s$  along the link attached to this particular joint shaft.

The link surface strain  $\epsilon$  and bending torque of a uniform link are related according to

$$\tau_L(x) = \frac{EI}{y_b} \epsilon(x). \quad (7)$$

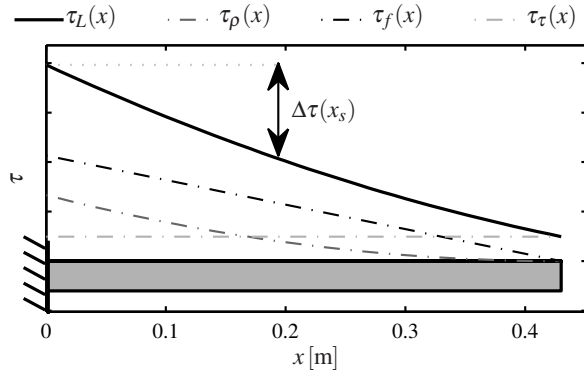


Fig. 3. The load torque distribution  $\tau_L(x)$  along a link (gray bar) can be expressed as the superposition of the three components  $\tau_p, \tau_f$  as well as  $\tau_\tau$ .

The symbol  $E$  denotes the Youngs modulus,  $I$  is the area moment of inertia about the bending axis whereas  $y_b$  is the distance between the link surface and the neutral fibre.

Consider a uniform massless cantilever as sketched in Fig. 3 subject to a constant load force  $f_L$  at the end. For a robot link, such a load force originates from the weight of subsequent links, a payload or a contact force. The torque distribution  $\tau_f(x)$  due to this force computes to

$$\tau_f(x) = f_L \frac{L}{EI} \left(1 - \frac{x}{L}\right), \quad (8)$$

where  $L$  represents the beam length.

Next, consider the same massless cantilever with a constant bending torque  $\tau_b$  at the tip. Regarding robot links, such a torque may arise from the weights of distal links and payloads or as a result from a contact situation. In this case the torque distribution  $\tau_\tau(x)$  is constant along the link:

$$\tau_\tau(x) = \tau_b \frac{1}{EI}. \quad (9)$$

Finally, consider a load free cantilever with the mass density per unit length  $\rho_b$ . This load is due to the weight of the link itself. The associated torque distribution  $\tau_p(x)$  is computed by

$$\tau_p(x) = \rho_b \frac{L^2}{2EI} \left(1 - 2\frac{x}{L} + \left(\frac{x}{L}\right)^2\right). \quad (10)$$

Under the assumption of small deflections, the differential equations of motion describing the link bending are linear [5] and can be superimposed to yield the complete torque distribution in the link:

$$\tau_L(x) = \tau_p(x) + \tau_f(x) + \tau_\tau(x). \quad (11)$$

This equation generally describes the load conditions for any arbitrary uniform link in the kinematic chain of a robot arm. The individual torque contributions as well as the superposition is sketched in Fig. 3.

The difference  $\Delta\tau$  between the torque  $\tau_L(0)$  at the joint and the torque  $\tau_L(x_s)$  at the strain gauge location  $x_s$  computes to:

$$\Delta\tau = \tau_L(0) - \tau_L(x_s) = \frac{\rho_b}{EI} \left(x_s L - \frac{1}{2}x_s^2\right) + \frac{f_L}{EI}x_s. \quad (12)$$

The first summand in this equation is constant. The second summand depends on the load force  $f_L$ . For any joint configuration of the subsequent links in the chain, this force remains the same. Orientation changes of the link under consideration equally scale all components of equation (11) and therefore cancel out. As a consequence, in the presence of a constant payload and in the absence of external contact forces, the difference  $\Delta\tau_L$  is therefore constant as well. Under this condition there exists a linear mapping between the strain  $\varepsilon$  measured at a location  $x_s$  along the link and the load torque  $\tau_J = \tau_L(0)$  acting on the joint shaft. Combining equations (7) and (12), this mapping is

$$\tau_J = \frac{EI}{y_b} \varepsilon(x_s) + \Delta\tau. \quad (13)$$

Due to the linearity of this mapping, the effect of link motions on the perceived surface strain can be described analogously to equation (5) by using exactly the same mathematical structure

$$\boldsymbol{\varepsilon}(\mathbf{x}_s) = \mathbf{I}_\varepsilon(\mathbf{q})\ddot{\mathbf{q}} + \mathbf{C}_\varepsilon(\mathbf{q}, \dot{\mathbf{q}})\dot{\mathbf{q}} + \mathbf{g}_\varepsilon(\mathbf{q}), \quad (14)$$

where the subscript  $\varepsilon$  indicates the reference to the strain measurements. A linear regression problem similar to equation (6) can be formulated with respect to the link strains:

$$\boldsymbol{\varepsilon} = \mathbf{Y}_\varepsilon(\mathbf{q}, \dot{\mathbf{q}}, \ddot{\mathbf{q}}) \boldsymbol{\chi}_\varepsilon. \quad (15)$$

The key difference between the equations (6) and (15) is that the latter excludes the joint parameters, most importantly the joint friction. Joint friction torques can not be measured directly. They have to be observed. The parameters of equation (2) frequently vary over time due to temperature dependencies, changes in lubrication, wear and tear [9]. A link strain referred dynamics model such as equation (14) assesses the actual mechanical load set free from the joint friction. The links with the applied strain gauges resemble load side torque sensors.

### C. The Data-driven Model

A fast learning scheme for feed-forward neural networks, which is known as Extreme Learning Machine (ELM, [10], see Fig. 4), is applied to model the elastic arm dynamics from data without prior structural knowledge of the system. In principle, any other machine learning approach for non-linear function approximation could be applied. However, ELMs are trained very efficiently in one shot by linear regression and typically achieve excellent generalization results [11].

ELMs combine a non-linear and high-dimensional random projection of inputs  $\mathbf{u} \in \mathbb{R}^D$  into a hidden layer  $\mathbf{h} \in \mathbb{R}^{H \gg D}$  with efficient linear regression learning of a linear read-out layer  $\mathbf{W}^{\text{out}}$ . The outputs  $\mathbf{v}$  are calculated according to

$$\mathbf{v} = \mathbf{W}^{\text{out}} \mathbf{h}(\mathbf{u}) = \mathbf{W}^{\text{out}} \boldsymbol{\sigma}(\mathbf{W}^{\text{inp}} \mathbf{u}), \quad (16)$$

where  $\boldsymbol{\sigma}(a_i) = (1 + \exp(-a_i - b_i))^{-1}$  are sigmoidal activation functions applied to the neural activities  $a_i = \sum_{j=1}^D (\mathbf{W}^{\text{inp}})_{ij} u_j$  for all hidden neurons  $i = 1, \dots, H$ .

Learning is restricted to the read-out weights  $\mathbf{W}^{\text{out}}$ . The input weights  $\mathbf{W}^{\text{inp}}$  and biases  $b_i$  are randomly initialized

TABLE I  
IDENTIFICATION RESULTS FOR THE ANALYTICAL (AN) AS WELL AS THE ELM MODEL WITH PAYLOADS  $m_L = 0 \dots 400$  g.

$m_L$	[g]	ELM	AN	ELM	AN	ELM	AN	ELM	AN	ELM	AN
		0		100		200		300		400	
link strain models											
Training											
RMSE	$[\mu\text{m}/\text{m}]$	12.19	13.11	18.15	19.93	24.86	28.30	28.48	31.83	47.65	53.77
$\sigma(E)$	$[\mu\text{m}/\text{m}]$	14.22	16.04	18.60	20.63	30.76	33.44	30.22	34.61	62.20	67.19
fit	[%]	92.26	91.44	90.40	89.41	87.16	85.83	87.71	86.03	80.07	78.05
Testing											
RMSE	$[\mu\text{m}/\text{m}]$	17.76	14.92	26.72	25.77	28.86	27.73	33.36	32.36	57.27	54.71
$\sigma(E)$	$[\mu\text{m}/\text{m}]$	21.84	17.44	40.54	32.45	32.11	27.85	34.92	32.97	78.35	69.44
fit	[%]	88.30	90.59	82.02	84.59	86.58	87.75	85.28	85.88	76.02	77.78
joint current models											
Training											
RMSE	[A]	0.11	0.12	0.16	0.19	0.13	0.17	0.20	0.22	0.22	0.24
$\sigma(E)$	[A]	0.07	0.07	0.11	0.10	0.09	0.08	0.13	0.12	0.15	0.14
fit	[%]	71.02	69.32	57.99	53.36	69.19	38.60	62.97	59.36	63.53	61.28
Testing											
RMSE	[A]	0.15	0.13	0.20	0.19	0.23	0.22	0.23	0.22	0.28	0.26
$\sigma(E)$	[A]	0.10	0.08	0.16	0.11	0.23	0.12	0.14	0.13	0.46	0.16
fit	[%]	58.92	63.96	50.13	55.65	47.62	52.75	54.50	54.78	40.21	56.96

according to a uniform distribution in  $[-1, 1]$  and remain fixed. Learning of  $\mathbf{W}^{\text{out}}$  proceeds off-line by linear regression. For all training samples  $\mathbf{u}_k$  with  $k = 1, \dots, K$ , the hidden states  $\mathbf{h}(\mathbf{u}_k)$  as well as the target outputs  $\mathbf{v}_k$  are collected in matrices  $\mathbf{U}$  and  $\mathbf{V}$ , respectively. Then, the optimal read-out weights are given by the least squares solution

$$\mathbf{W}^{\text{out}} = (\mathbf{U}^T \mathbf{U} + \lambda \mathbf{1})^{-1} \mathbf{U}^T \mathbf{V}, \quad (17)$$

where  $\mathbf{1}$  is the identity and  $\lambda > 0$  a regularization parameter. Inputs and outputs are normalized to the range  $[-1, 1]$  according to the distribution of the training data. This yields to good learning results without further tuning of parameters.  $H = 100$  hidden neurons and  $\lambda = 10^{-6}$  in (17) are used.

#### IV. IDENTIFICATION OF AN ELASTIC LINK ROBOT ARM

##### A. Training

Over decades a huge amount of work has been carried out concerning the generation of optimal excitation signals for the dynamics identification of robot arms [12]. To mention just a few, the authors of [13] propose to use a bandlimited periodic sinusoidal parametrized as a finite Fourier series. This elegantly allows for simple computation of higher order measurement derivatives in the presence of noise. Earlier works investigate excitation trajectory optimization criteria

such as the condition numbers and singular values of the regression matrices [14].

In this contribution the identification of both the analytical model as well as the data-driven model is based on amplitude-modulated pseudo-random binary stimuli (APRBS) [15, p. 174] generated for the joint angles. The APRBS signal is a general purpose excitation stimulus for the identification of non-linear systems. It suits well for the training of the ELM reference network and results in sufficiently good condition numbers and smallest singular values of the regression matrices  $\mathbf{Y}_i$  and  $\mathbf{Y}_e$  for the analytical model.

The stimuli are generated for the second and third joint individually, but executed on both joints simultaneously. This work focuses on the modelling of the damped elastic links. Therefore, the first joint is kept at zero position without loss of generality. All stimuli have a duration of 80 s. Responses are recorded at a sampling rate of 100 Hz and subsampled to 20 Hz for identification. This amounts to  $N = 1600$  data points per stimulus. The modulation bandwidth for the joint angle amplitudes is  $0 \dots 1$  Hz. The modulated amplitudes are equally distributed in the entire operating range provided in Fig. 1. An online joint-space trajectory planner converts the rectangular shaped joint angle stimuli into joint trajectories based on a smooth  $\sin^2$  acceleration profile. The profile shows no impulsive jerk and protects the gears. The maximum acceleration is  $200 \text{ deg/s}^2$ . The maximum speed is  $70 \text{ deg/s}$ . Figure 5 exemplifies two such joint stimulus responses for the second joint.

In total 10 joint position stimulus responses are recorded for each payload between  $m_L = 0 \dots 400$  g. The data is randomly split into 50 % for training and 50 % for testing. The analytical and data-driven models are trained for each payload individually.

The analytical as well as the data-driven model share the same inputs and outputs. The inputs are  $\mathbf{u} = [\theta_2, \theta_3, \dot{\theta}_2, \dot{\theta}_3, \ddot{\theta}_2, \ddot{\theta}_3]^T$ . The joint velocities are obtained from numerical differentiation and filtering with a first order filter

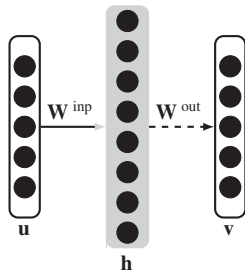


Fig. 4. Extreme Learning Machine (ELM).



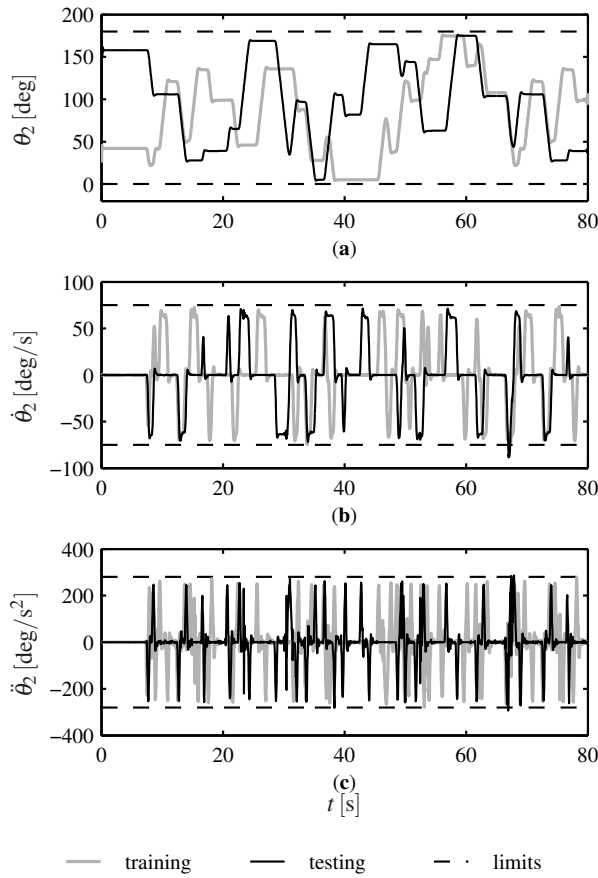


Fig. 5. Joint angle (a), angular velocity (b) and acceleration (c) responses exemplified for two joint stimulus responses.

and a cut-off frequency of 80 Hz. The joint accelerations are obtained from a subsequent numerical differentiation filtering of the velocity signal with a cut-off frequency of 20 Hz. The outputs are either the actuator currents  $\mathbf{v} = [i_{M,2}, i_{M,3}]^T$  for the joint current models or the strains measured close to the joint hubs on the elastic links  $\mathbf{v} = [\varepsilon_2, \varepsilon_3]^T$  for the link strain models.

### B. Testing

Table I summarizes the training and testing results for both the joint current models as well as the link strain models and all payloads. It contains the root mean squared error (RMSE) aggregated on both dimensions of the measurement vector  $\mathbf{v}$  and model output  $\hat{\mathbf{v}}$  along with the corresponding standard deviation of the error  $\sigma(E)$ . A closer look at the error histogramms (not shown) reveals that the modelling errors are indeed normally distributed with close to zero mean. Additionally table I provides the goodness of fit metric. The goodness of fit reflects the percentage of the standard deviation in a reference signal  $\mathbf{v}$  explained by the model output  $\hat{\mathbf{v}}$  and is computed by

$$\text{fit} := 100 \left( 1 - \frac{\|\mathbf{v} - \hat{\mathbf{v}}\|}{\|\hat{\mathbf{v}} - \bar{\mathbf{v}}\|} \right), \quad [\%]. \quad (18)$$

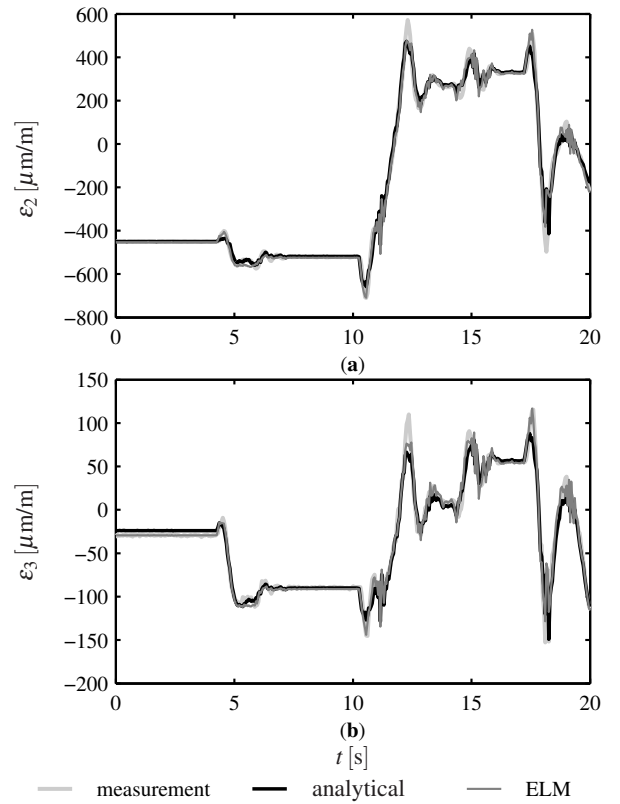


Fig. 6. Example testing result for the strains measured on the second (a) and third (b) link for  $m_L = 400$  g.

The bar indicates the mean over all values. A model that produces a goodness of fit metric above 80 % is commonly accepted as a good model.

For the analytical link strain model basically reaches well above the goodness of fit metric of 80 %. For payload  $m_L = 0$  g it even reaches 90 %. Only for  $m_L = 400$  g it falls slightly below the 80%. Figure 6 shows an exemplary identification result for a stimulus part of the test set. The analytical model as well as the ELM model almost coincide. Generally both curves reliably track the measurement. Deviations between the measurements and the model basically originate from measurement noise and imperfect oscillation damping. The imperfect oscillation damping is visible in Fig. 6 (a) and (b) during the small motions around second 5. For heavier payloads the rapid direction reversal causes the strain peaks partially explained by the models at 12 s and 18 s.

The joint current models both show lower fit metrics. The reason for that is suspected to be the reduced signal to noise ratio of the current measurements along with unmodelled joint friction effects. Especially the analytical model reacts quite sensitive to measurement noise during steady states as visible in Fig. 7 (a) and (b). The reason for that are the velocity direction dependencies of the coulomb friction model. During motions, the joint current identification results are comparable to the link strain results.

The ELM link strain model shows an approximately 2 %

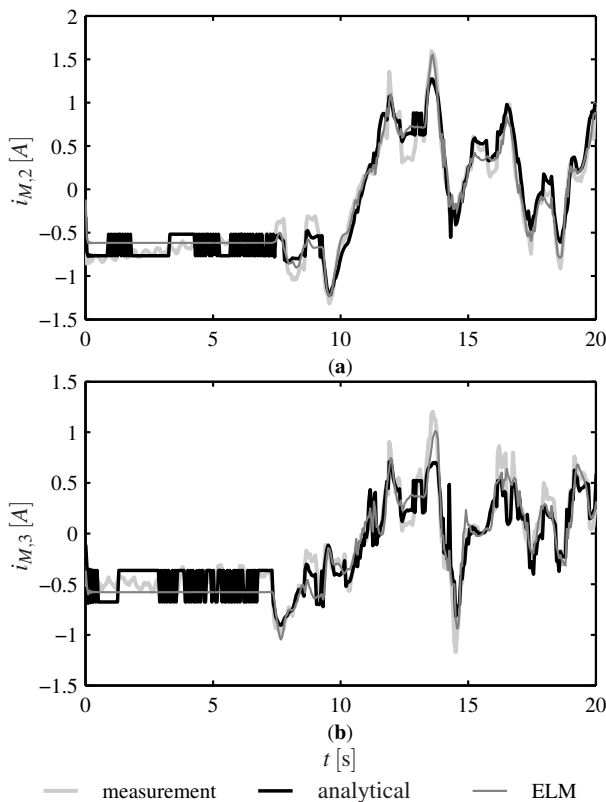


Fig. 7. Example testing result for the motor currents measured in the second (a) and third (b) joint for  $m_L = 400$  g.

more accurate fit on the training data compared to the analytical model. On the other hand, the analytical link strain model shows almost the same 2% improvement compared to the ELM on the test data. Equivalent observations can be made for the joint current models. In accordance with zero centered gaussian error histogramms, the small difference between analytical and data-driven model additionally confirms that the proposed analytical model structure is valid to explain the relevant effects in the strain measurements of the damped multi elastic link robot. In conclusion, analytical models – if available – should be preferred, while data-driven models nevertheless constitute valuable alternatives, which can reduce modeling efforts and computational complexity.

## V. CONCLUSIONS AND OUTLOOK

This work shows that, once the structural oscillations are properly damped by an inner loop controller, the remaining link strain dynamics of a multi elastic link robot arm can be modelled using exactly the same model structure as the joint current referred model known from conventional rigid robots. The findings have been validated based on extensive dynamic motion experiments using different payloads and a data-driven reference model. The work avoids an accurate solution of the beam partial differential equation based on possibly unknown boundary conditions and circumvents common control problems with elastic link robots. The proposed models can be employed in real-time control such that the

proposed approach is a starting point for future online payload estimation and consequently improved load adaptation of the inner controllers. This contribution makes a major step from considering link elasticity “just as a problem” to enabling the exploitation of intrinsic link compliance for the development of force controllers.

The authors provide an online available **video** (<http://youtu.be/kJPuenyxeps>) demonstrating the practical use of their analytical model for collision detection and reaction with their experimental setup TUDOR.

## ACKNOWLEDGMENT

All authors contributed to research design and writing paper. J.M. conducted the core research on analytical modeling, robotic experiments, and evaluation. He has been funded by the German Research Foundation (DFG, BE 1569/7-1). R.F.R. conducted the data-driven modelling and evaluation. R.F.R. is funded by the German BMBF within the Intelligent Technical Systems Leading-Edge Cluster Competition and managed by the Project Management Agency Karlsruhe.

## REFERENCES

- [1] G. Dubus, O. David, and Y. Measson, “Vibration Control of a Flexible Arm for the ITER Maintenance Using Unknown Visual Features From Inside the Vessel,” in *IEEE/RSJ International Conference on Intelligent Robots and Systems (IROS)*, 2009, pp. 5697–5704.
- [2] W. O Connor, F. La Ramos de Flor, D. McKeown, and V. Feliu, “Wave-based control of non-linear flexible mechanical systems,” *Non-linear Dynamics*, vol. 57, no. 1, pp. 113–123, 2009.
- [3] Xin Jiang, Y. Yabe, A. Konno, and M. Uchiyama, “Vibration Suppression Control of a Flexible Arm Using Image Features of Unknown Objects,” in *IEEE/RSJ International Conference on Intelligent Robots and Systems (IROS)*, 2008, pp. 3783–3788.
- [4] J. Malzahn, A. S. Phung, F. Hoffmann, and T. Bertram, “Vibration control of a multi-flexible-link robot arm under gravity,” in *International Conference on Robotics and Biomimetics (ROBIO)*, 2011, pp. 1249–1254.
- [5] L. Meirovitch, *Fundamentals of vibrations*. Boston: McGraw-Hill, 2001.
- [6] A. d. Luca and B. Siciliano, “Closed-form dynamic model of planar multilink lightweight robots,” *IEEE Transactions on Systems, Man and Cybernetics*, vol. 21, no. 4, pp. 826–839, 1991.
- [7] J. Malzahn, A. S. Phung, and T. Bertram, “A Multi-Link-Flexible Robot Arm Catching Thrown Balls,” in *7th German Conference on Robotics 2012*, 2012, pp. 1–6.
- [8] W. Khalil and E. Dombre, *Modeling, identification and control of robots*. Butterworth-Heinemann, 2004.
- [9] B. Bona and M. Indri, “Friction compensation in robotics: an overview,” in *44th IEEE Conference on Decision and Control and European Control Conference. CDC-ECC’05*, 2005, pp. 4360–4367.
- [10] G.-B. Huang, Q.-Y. Zhu, and C.-K. Siew, “Extreme learning machine: a new learning scheme of feedforward neural networks,” in *IEEE Intern. Joint Conf. on Neural Networks*, vol. 2, 2004, pp. 985–990.
- [11] K. Neumann, C. Emmerich, and J. J. Steil, “Regularization by Intrinsic Plasticity and its Synergies with Recurrence for Random Projection Methods,” *Journal of Intelligent Learning Systems and Applications*, vol. 4, no. 3, pp. 230–246, 2012.
- [12] B. Armstrong, “On finding exciting trajectories for identification experiments involving systems with nonlinear dynamics,” *The International Journal of Robotics Research*, vol. 8, no. 6, pp. 28–48, 1989.
- [13] J. Swevers, W. Verdonck, and J. d. Schutter, “Dynamic model identification for industrial robots,” *Control Systems, IEEE*, vol. 27, no. 5, pp. 58–71, 2007.
- [14] C. Presse and M. Gautier, “New criteria of exciting trajectories for robot identification,” in *Proceedings of the IEEE International Conference on Robotics and Automation*, 1993, pp. 907–912.
- [15] R. Isermann and M. Münchhof, *Identification of dynamic systems: An introduction with applications*. Heidelberg and New York: Springer, 2011.